

SCIENTIFIC REPORTS



OPEN

Imaging Shock Waves in Diamond with Both High Temporal and Spatial Resolution at an XFEL

Received: 11 February 2015

Accepted: 01 May 2015

Published: 18 June 2015

Andreas Schropp¹, Robert Hoppe², Vivienne Meier^{2,*}, Jens Patommel², Frank Seiboth², Yuan Ping³, Damien G. Hicks^{3,4}, Martha A. Beckwith³, Gilbert W. Collins³, Andrew Higginbotham^{5,**}, Justin S. Wark⁵, Hae Ja Lee⁶, Bob Nagler⁶, Eric C. Galtier⁶, Brice Arnold⁶, Ulf Zastrau⁶, Jerome B. Hastings⁶ & Christian G. Schroer^{1,†}

The advent of hard x-ray free-electron lasers (XFELs) has opened up a variety of scientific opportunities in areas as diverse as atomic physics, plasma physics, nonlinear optics in the x-ray range, and protein crystallography. In this article, we access a new field of science by measuring quantitatively the local bulk properties and dynamics of matter under extreme conditions, in this case by using the short XFEL pulse to image an elastic compression wave in diamond. The elastic wave was initiated by an intense optical laser pulse and was imaged at different delay times after the optical pump pulse using magnified x-ray phase-contrast imaging. The temporal evolution of the shock wave can be monitored, yielding detailed information on shock dynamics, such as the shock velocity, the shock front width, and the local compression of the material. The method provides a quantitative perspective on the state of matter in extreme conditions.

Whilst many of the advances afforded by x-ray free-electron lasers (XFELs)^{1–3} are completely new^{4–6}, several key results have been obtained by exploiting established static techniques and transporting them to the femtosecond time-domain made possible by the short duration of the XFEL pulses^{7,8}. Hard x-ray phase-contrast imaging (PCI), an established technique at modern synchrotron radiation sources, enables one to image optically opaque samples with high spatial resolution^{9–11}. Its sensitivity to the phase shift introduced by an object enhances the visibility of structures otherwise invisible in x-ray radiography based on absorption^{12,13}. When combined with the femtosecond duration of an XFEL pulse, such a technique allows imaging of matter changing rapidly in both space and time. We make use of the very short but intense XFEL pulses to image the propagation of an elastic compression wave in diamond with both high temporal (~50 fs pulse duration) and spatial resolution (~500 nm). As shock waves in matter typically travel at speeds in the range of several kilometers per second, x-ray pulses in the picosecond regime are required to freeze the motion of the shock wave. We developed a new x-ray microscope based on beryllium compound refractive x-ray lenses (Be CRLs)¹⁴, which is especially optimized for the XFEL environment and can withstand the full XFEL beam¹⁵. The x-ray microscope is part of an infrared-laser-pump-x-ray-probe setup. It generates shock waves in matter using a short optical laser

¹Deutsches Elektronen-Synchrotron DESY, Notkestr. 85, D-22607 Hamburg, Germany. ²Institute of Structural Physics, Technische Universität Dresden, D-01062 Dresden, Germany. ³Lawrence Livermore National Laboratory, 7000 East Avenue, Livermore, CA 94550, USA. ⁴Centre for Micro-Photonics, Swinburne University of Technology, Hawthorn, VIC 3122, Australia. ⁵Department of Physics, Clarendon Laboratory, University of Oxford, Parks Road, Oxford OX1 3PU, United Kingdom. ⁶Linac Coherent Light Source, SLAC National Accelerator Laboratory, 2575 Sand Hill Road, Menlo Park, CA 94025, USA. *Current address: Institute of Integrative Nanosciences, IFW Dresden, Helmholtzstr. 20, D-01069 Dresden, Germany. **Current address: York Plasma Institute, Department of Physics, University of York, Heslington, York YO 5DD, United Kingdom. †Current address: Department Physik, Universität Hamburg, Luruper Chaussee 149, D-22761 Hamburg, Germany. Correspondence and requests for materials should be addressed to A.S. (email: andreas.schropp@desy.de)

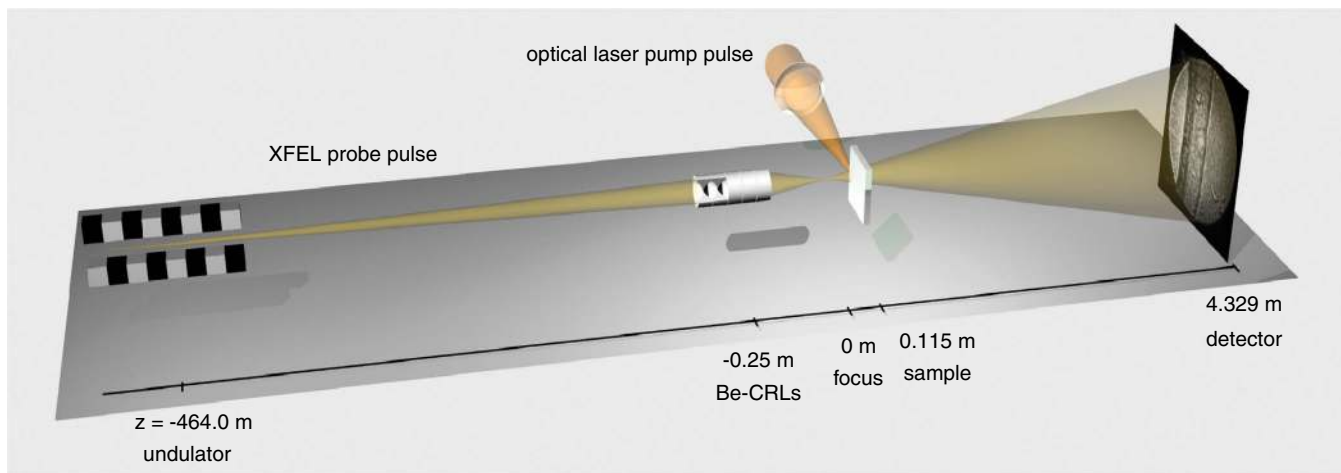


Figure 1. Schematic outline of the optical setup used for magnified x-ray phase-contrast imaging. Optical axis is not to scale.

pulse and probes the sample state using magnified phase-contrast imaging with a single XFEL pulse. From these images, we can quantitatively reconstruct the density profiles and thus infer the state immediately behind the shock front.

The extreme physical properties of diamond make it a material of enduring scientific and technological interest. Its unique combination of ultra-high stiffness, hardness, optical transparency, and thermal conductivity have made it a focal point of high-pressure science for decades. Several recent publications have examined the behaviour of diamond under dynamic compression from 0.1 TPa to 5 TPa^{16–20}. All these studies used optical interferometry to infer conditions in the compression wave. Here for the first time we directly image the shock wave using x rays, opening up a valuable new perspective on the dynamic behaviour of diamond under high pressure.

The experiment was carried out at the Matter in Extreme Conditions (MEC) endstation of the Linac Coherent Light Source (LCLS) XFEL. The instrument is located in the far-experimental hall at a distance of about 464 m from the undulator x-ray source (cf. Fig. 1). The x-ray microscope is based on a magnified inline imaging scheme that requires the creation of a secondary source using x-ray optics^{12,21}. At a photon energy of 8.2 keV a stack of 20 Be CRLs focuses the LCLS beam to a spot with a size of 125 nm full width at half maximum (FWHM) at a focal length of 250 mm behind the optics²².

The diamond samples (cf. Sample preparation in the Methods) were positioned at a distance of $z_s = 115$ mm behind the focus. The magnified near-field images of the samples were projected onto a detector located at $z_d = 4214$ mm behind the sample (cf. Fig. 1), yielding a magnification of $M = 37.6$ ¹⁵. The method requires a high degree of spatial but only a moderate degree of longitudinal coherence²³. These requirements are well matched by the beam characteristics of an XFEL based on self-amplified spontaneous emission (SASE), such as those at the LCLS^{24,25}. The shock wave was induced in the diamond samples by shining an 800 nm-infrared laser with a pulse duration of 150 ps (FWHM) onto the sample from the side (cf. Optical laser in the Methods).

Figure 2 shows a series of phase-contrast images measured at different time delays ranging from 1.2 ns in Fig. 2(a) to 3.0 ns in Fig. 2(d). These images clearly show the decay of the elastic compression wave during the 3 ns time interval producing less contrast towards the longer time delays. Since the target area is destroyed by the high-intensity optical laser pulse, each of these images was taken at a fresh spot on the sample or even different diamond samples.

To obtain quantitative measurements of the density in the shock front and its velocity we model the image formation process that leads to the images in Fig. 2(a–d). The transmission of the x rays through the thin object is described by a complex transmission function $O(\mathbf{r})$ that relates the transmitted wave field $\psi(\mathbf{r})$ to the wave field $P(\mathbf{r})$ incident on the sample by $\psi(\mathbf{r}) = O(\mathbf{r}) \cdot P(\mathbf{r})$. The transmitted wave field then propagates to the detector. In the paraxial approximation the propagation is modeled by the Fresnel-Kirchhoff integral²⁶. By recording the intensity in the detector plane, the phases of the x-ray wave field are lost. With the knowledge of the incident wave field obtained by an antecedent beam-characterization experiment (ptychography)²² the transmission function $O(\mathbf{r})$ can be reconstructed by phase-retrieval techniques (cf. Data analysis in the Methods). In this way image distortions related to phase modulations in the incident wave front can be corrected for. Such distortions, which are due to aberrations of the lens or other defects, are visible for example in Fig. 2(b) (marked by arrows). The compression of the material by the shock wave introduces an additional phase shift in the x-ray wave field behind the sample. Figure 2(e–h) depicts the phase maps [phase of the transmission function $O(\mathbf{r})$] in the sample plane obtained by iterative phase retrieval from Fig. 2(a–d), respectively.

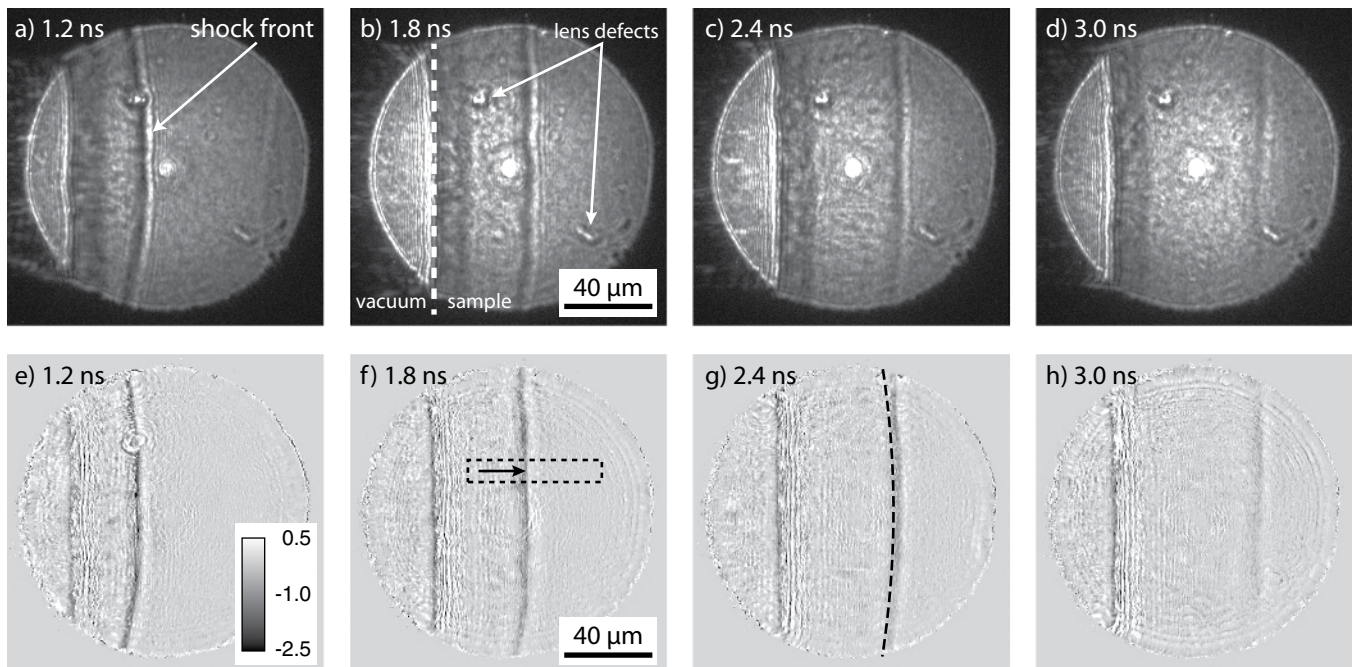


Figure 2. (a–d) Phase-contrast images measured with a high-resolution x-ray detector at a distance of 4214 mm behind the sample. Specific time delays are indicated in each image. (e–h) Corresponding phase maps obtained by iterative phase retrieval from the images above. In order to enhance the visibility of shock-related features, the phase map obtained from just the sample without shock wave was subtracted from the phase map with shock wave. Gray values indicate the phase shift in radians [cf. inset in Fig. e)]. In Fig. f) a rectangular box highlights the area used to quantitatively determine the compression of the material.

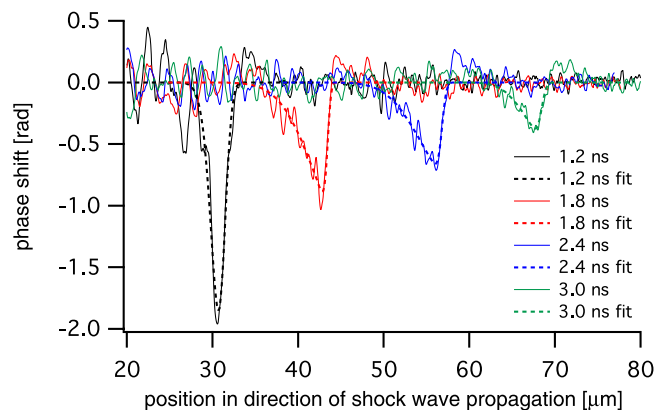


Figure 3. Phase profiles of the shock front at different time delays.

Figure 3 shows line profiles through the shock front extracted from Fig. 2(e–h) in an area highlighted by a dashed rectangle in Fig. 2(f). These profiles monitor the compression of the material in the propagating shock wave at the different time delays. The signal was averaged over a length of $10\mu\text{m}$ perpendicular to the propagation direction in order to reduce the influence of noise. By measuring the distance between the sample edge and the shock front, a shock velocity $v = (19.9 \pm 1.7) \text{ km/s}$ was determined (cf. Magnified phase-contrast imaging in the Methods).

The phase profiles shown in Fig. 3 are well represented by a double-sided error function as indicated by dashed lines. Since the reconstructed phase change corresponds to an integrated value accumulated along the path of the x rays through the sample, it is in general not proportional to the local compression of the material. In order to retrieve the compression quantitatively, further modeling of the shock wave inside the material is required. To this end, we assume a spherically curved wave front whose radius of curvature can be obtained from Fig. 2. Using tomographic reconstruction under the assumption of spherical symmetry, the local phase change $\Delta\varphi$ per voxel is reconstructed (cf. Data analysis in

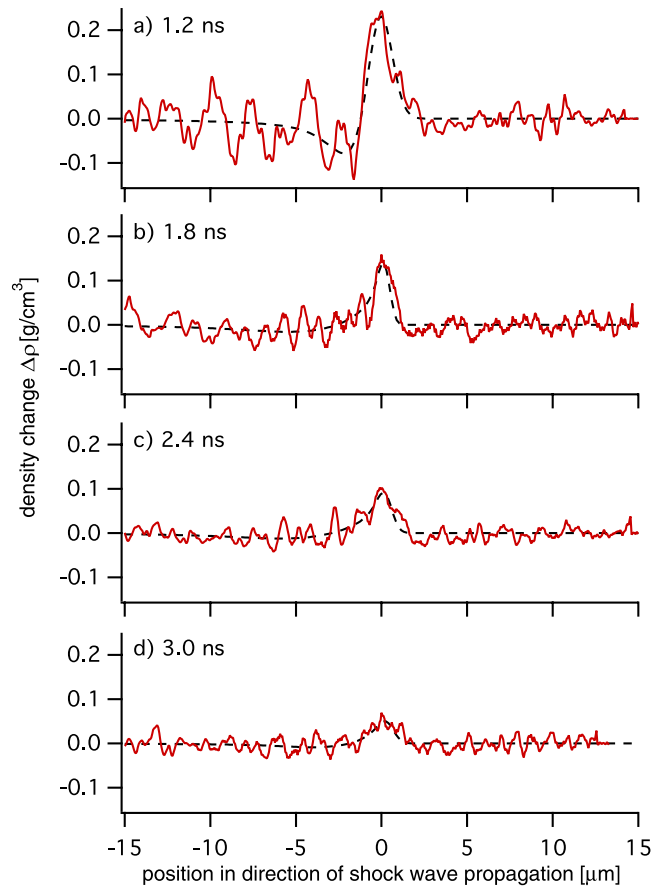


Figure 4. Density profiles of the shock front after the application of the tomographic reconstruction algorithm.

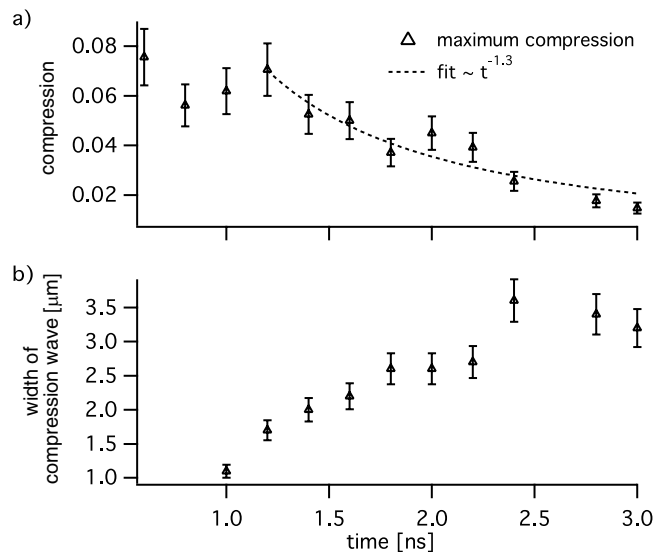


Figure 5. Decay of the elastic compression wave.

the Methods). In Fig. 4 line profiles monitoring the local change in density are summarized. They were obtained from the tomographically reconstructed phase profiles $\Delta\varphi$ by using $\Delta\rho = -\Delta\varphi/[kd(\delta/\rho)]$, where $\Delta\rho$ is the change in density, $k = 4.16 \times 10^7 \text{ mm}^{-1}$ the wave number, $d = 59.8 \text{ nm}$ the thickness of a cubic voxel, and $\delta/\rho = 3.1 \times 10^{-6} (\text{g/cm}^3)^{-1}$ the refractive index decrement δ normalized to the density ρ of the uncompressed material at the photon energy of $E = 8.2 \text{ keV}$.

As the compression wave propagates into the target (cf. Fig. 4), it decreases in amplitude and increases in width. This is due to the finite duration of the originally applied pressure pulse, which results in a rarefaction wave that releases the stress behind the shock front. In Fig. 5(a) the decay of the maximum compression C_{\max} as function of time t is shown. Specific compression values were determined using $C_{\max}(t) = \Delta\rho_{\max}(t)/\rho$, with $\rho = 3.52 \text{ g/cm}^3$ the bulk density of diamond. At the same time the shock width increases from about $1.5 \mu\text{m}$ to $3.5 \mu\text{m}$ in the given time window [cf. Fig. 5(b)]. Error bars in Fig. 5(b) indicate an 8.7% inaccuracy in shock width, which is related to the error in length scale in the phase-contrast images (cf. Magnified phase-contrast imaging in the Methods). The high sensitivity of PCI allows one to measure density variations as small as 1% in this case, and the early time steepening of the wave front is resolved for the first time with a sub-micron resolution. Numerical calculations confirm that for the applied pressure pulse the compression steepens up within the first nanosecond owing to the non-linear compressibility, such that the front itself has a width of order the lattice spacing. Although this sharp front can not be resolved with this setup, it can be used to determine the resolution power of the microscope. From the inferred compression, we conclude that this is a purely elastic wave, as the pressures are well below the Hugoniot elastic limit (HEL) of diamond¹⁸.

In this first approach to quantitatively analyze the phase-contrast images we determined a wave curvature of $R = 440 \mu\text{m}$ at the time delay of $\Delta t = 1.2 \text{ ns}$, which scales linearly up to $R = 476 \mu\text{m}$ at $\Delta t = 3.0 \text{ ns}$. However, as can be seen in Fig. 2(e–h) the precise shape of the elastic wave varies considerably between different pulses and, therefore, we make a conservative error estimate for the radius of curvature of approximately $\Delta R/R \approx 30\%$. Numerical simulations showed that this systematic error propagates into the determination of the material induced phase shift using tomography by $\Delta\varphi/\varphi \approx 0.5 \cdot \Delta R/R = 15\%$. Since density change $\Delta\rho$ and compression C are linearly related to this phase change, the same relative error holds for the deduced values, i. e., $\Delta\rho/\rho = \Delta C/C \approx 15\%$ [cf. error bars in Fig. 5(a)].

With this example, we demonstrated that fast dynamic processes inside matter can be visualized *in situ* with both high temporal and high spatial resolution by magnified x-ray phase-contrast imaging at an XFEL. Smallest visible features had a size of about 500 nm, mainly limited by the bandwidth of the XFEL beam. A seeded XFEL beam combined with an optimized detector setup will improve the resolution to better than 100 nm. Note that the temporal resolution, set by the x-ray pulse length, is shorter than even the fastest phonon period in the system, totally eliminating temporal blurring. This combination of spatial and temporal resolution could thus find a range of applications in shock physics, as this scale length is, for example, smaller than typical grain sizes in most polycrystalline samples, affording the possibility of observing the effect of grain boundaries and orientations on shock propagation. Furthermore, although the elastic compression wave here was atomic in front width, the direct observation of the evolution of the width of the front in a shock for a material subjected to pressures above the HEL would provide significant insight into the time scales for plastic flow under high strain-rate conditions well in excess of 10^9 s^{-1} .

Methods

Diamond samples. The diamond samples are optical grade polycrystalline strips with dimensions of $\Delta x \times \Delta y \times \Delta z = 30 \text{ mm} \times 145 \mu\text{m} \times 272 \mu\text{m}$. They are produced by chemical vapor deposition (CVD) and contain micrometer-sized grains. The LCLS beam, propagating in \vec{e}_z -direction, hits the polished side of the sample having less than 7 nm peak-to-valley roughness, whereas the shock-driving laser pulse is incident perpendicular to the LCLS beam onto the unpolished side of the sample propagating in $-\vec{e}_y$ -direction. The elastic wave therefore propagates in $-\vec{e}_y$ -direction. The x-ray transmission image is recorded through the $272 \mu\text{m}$ -thick side of the sample.

Optical laser. The shock wave was initiated by a Gaussian-shaped, 150 ps (FWHM) drive laser with a wavelength $\lambda = 800 \text{ nm}$ and energy $E = 130 \text{ mJ}$ per pulse. The optical beam was focused onto the diamond target to a spot with a size of $80 \mu\text{m}$ (FWHM), which corresponds to a maximum peak power of $P \approx 12 \text{ TW/cm}^2$.

Magnified phase-contrast imaging. The experiment was carried out in a magnified inline geometry. By using a set of 20 Be CRLs a secondary x-ray source was created at $z_s = 115 \text{ mm}$ in front of the sample²². The area of the sample illuminated by the divergent x-ray beam was imaged onto a high-resolution x-ray detector positioned at a distance of $z_d = 4214 \text{ mm}$ after the sample, resulting in a magnification of $M = (z_s + z_d)/z_s = 37.6$. The scintillator-based high-resolution detector has an effective pixel size of $p_d = 2.25 \mu\text{m}$, leading to $p = p_d/M = 59.8 \text{ nm}$ pixels in the phase-contrast images. This experimental arrangement with spherical-wave illumination is equivalent to a plane wave geometry with an effective propagation distance of $z_{\text{eff}} = z_d/M = 112 \text{ mm}$ ^{12,13,27}. The error in magnification ΔM is related to measurement inaccuracies of the distance values z_s and z_d . It is given by $\Delta M/M = |z_d/(z_s + z_d)| \cdot (\Delta z_s/z_s + \Delta z_d/z_d) \approx \Delta z_s/z_s + \Delta z_d/z_d$, if $z_s \ll z_d$. In this case, it further reduces to $\Delta M/M \approx \Delta z_s/z_s$, since the relative error in z_d was much smaller than the error in z_s . The distance z_s could be calibrated with an accuracy of approximately $\Delta z_s = 10 \text{ mm}$, yielding a relative error in magnification and the corresponding length scale in the phase-contrast images of 8.7%. Since the shock velocity was determined by measuring the

distance between the shock front and sample edge, this error propagates into the determination of the shock velocity, yielding finally $v = (19.9 \pm 1.7)$ km/s. Timing inaccuracies can be neglected, since the pulse-to-pulse jitter was only 300 fs and long-term drifts were smaller than 1 ps.

The spatial resolution of the method is mainly limited by the pixel size of the detector and the bandwidth of the incoming x-ray radiation. The slight polychromaticity reduces the contrast for high spatial frequencies. For a SASE bandwidth of $\Delta\lambda/\lambda = 2 \cdot 10^{-3}$, we expect a reduction in phase-contrast transfer by 50% or more for a spatial frequency above $u_{\max} = 5440 \text{ mm}^{-1}$, corresponding to a length scale of $d_{\min} \approx 200 \text{ nm}^{28}$. In addition, the chromaticity of the refractive lens leads to a slight blur ($\Delta f \approx 1 \text{ mm}$) of the focus position along the optical axis²⁹. Whereas this effect does not reduce the phase contrast for sample features located close to the optical axis, the smearing of the phase-contrast image becomes stronger towards larger angles and reaches a maximum of approximately 600 nm at the edge of the circular field of view.

Data analysis. The reconstruction scheme is based on the Hybrid-Input-Output (HIO) algorithm^{30,31}, making use of the additional knowledge of the complex-valued illumination function $P(\mathbf{r})$ characterized by ptychography in an antecedent experiment^{22,32}. The knowledge of $P(\mathbf{r})$ is necessary to disentangle contrast introduced by the sample from wave-field structures already present in the incoming x-ray beam. Like computational spectacles, it corrects the spherical aberration of the Be CRLs. As described in the previous section, the conical imaging geometry is equivalent to a parallel-beam geometry with a propagation distance of $z_{\text{eff}} = z_d/M = 112 \text{ mm}$ between object and detector plane.

We reconstruct the object-transmission function $O(\mathbf{r})$ iteratively: as a first guess $O_1(\mathbf{r})$ we use the reconstructed hologram. It is obtained by propagating the reconstructed probe function $P(\mathbf{r})$ (obtained with ptychography) to the image plane, subsequent pointwise multiplication with the real-valued phase-contrast image $I(\mathbf{r})$, propagating it back to the sample plane, and dividing the result by the complex probe function, i. e., $O_1(\mathbf{r}) = P^*(\mathbf{r}) / (|P(\mathbf{r})|^2 + \varepsilon) \cdot \{I \cdot [P(\mathbf{r})]\}$, where \mathcal{F}_d is the Fresnel propagator in paraxial approximation and ε a small regularizing constant. The central part of the phase-contrast image that contains a strong contribution from higher-harmonic radiation [bright spot at the center of Fig. 2(a–d)] was masked and set constant.

This step is followed by an iterative refinement of the object-transmission function based on a ptychographic algorithm³³, but using just a single phase-contrast image. The complex transmission function behind the sample in a certain iteration j is given by

$$\psi_j(\mathbf{r}) = P(\mathbf{r}) \cdot O_j(\mathbf{r}), \quad (1)$$

which is then propagated to the image plane

$$\Psi_j(\mathbf{r}) = \mathcal{F}_d[\psi_j(\mathbf{r})]. \quad (2)$$

Here, the amplitude of the wave field is replaced by the measured phase-contrast imaging data $I(\mathbf{r})$

$$\Psi'_j(\mathbf{r}) = \sqrt{I(\mathbf{r})} \cdot \frac{\Psi_j(\mathbf{r})}{|\Psi_j(\mathbf{r})|}. \quad (3)$$

The back propagation to the sample plane yields an updated transmitted wave field

$$\psi'_j(\mathbf{r}) = \mathcal{F}_d^{-1}[\Psi'_j(\mathbf{r})], \quad (4)$$

and the updated object function O_{j+1} is obtained by³³

$$O_{j+1}(\mathbf{r}) = O_j(\mathbf{r}) + a \cdot \frac{P^*(\mathbf{r})}{|P(\mathbf{r})|_{\max}^2} \cdot (\psi'_j(\mathbf{r}) - \psi_j(\mathbf{r})), \quad (5)$$

where the constant parameter a was set to 1. In a last step, the phase of the object function was constrained to the interval $[-\pi, 0]$ and, since the sample was composed of just a single material, the amplitude $A(\mathbf{r})$ of the object function was moderately coupled to the phase shift $\varphi(\mathbf{r})$ ³⁴. If $O(\mathbf{r}) = A(\mathbf{r})e^{i\varphi(\mathbf{r})}$, then

$$A'_{j+1}(\mathbf{r}) = e^{[(1-b)\ln A_{j+1}(\mathbf{r}) + bc\varphi_{j+1}(\mathbf{r})]}, \quad (6)$$

where $b = 0.6$ was set constant, and $c = \beta/\delta$ defines the material dependent coupling parameter between absorption and refraction. The parameters $\delta = 1.09 \times 10^{-5}$ and $\beta = 1.58 \times 10^{-8}$ describe the refractive index decrement and the attenuation in the refractive index $n = 1 - \delta + i\beta$ for diamond at $E = 8.2 \text{ keV}$, respectively. Convergence was achieved after 100 iterations.

This procedure was carried out for phase-contrast images of the sample without and with the elastic shock wave at different time delays in the pump-probe experiment. The phase map without the elastic

time delay	a_0 [rad]	a_1 [μm]	a_2 [μm]	a_3 [μm]	a_4 [μm]
1.2 ns	-6.43	31.1	0.06	1.37	0.7
1.8 ns	-1.59	42.8	1.23	3.45	0.3
2.4 ns	-1.00	55.7	2.30	3.29	0.4
3.0 ns	-0.62	67.7	1.56	2.35	0.1

Table 1. Summary of fit parameters.

wave was then subtracted from the phase map with the shock wave. The resulting phase maps are shown in Fig. 2(e–h) and were the basis for further analysis.

The extracted line profiles were fitted by a double sided error function of the form $f(x) = a_0/2 \cdot (1 + \text{erf}((x - a_1 + a_2/2)/(\sqrt{2} a_3)))(0.5 - 0.5 \text{erf}((x - a_1 - a_2/2)/(\sqrt{2} a_4)))$, with fit parameters a_0 , a_1 , a_2 , a_3 , and a_4 (cf. dashed lines in Fig. 3). The function well represents the extracted phase profiles and specific fit parameter values are summarized in Table 1.

In order to retrieve quantitative compression values the line profiles were further evaluated by standard tomographic techniques assuming a spherical distribution of compressed material. The curvature of the wave was determined directly from the image as indicated by a dashed line in Fig. 2(g). This assumes that the elastic wave is curved isotropically. In general, this assumption may be invalid, for example, when the density distribution is more complex. Here, however, the data do not indicate such a behavior. In the future, we want to investigate anisotropy effects in more complex materials.

The phase profiles and their fits, which are shown in Fig. 3, served as input data for tomographic reconstruction that finally yields the phase shift per cubic voxel with a volume of $(59.8)^3 \text{nm}^3$. This phase shift can then be transferred into compression $\Delta\rho/\rho$ as explained in the main text. The result of the tomographic analysis is summarized in Fig. 4. The red solid lines refer to data profiles and dashed black lines to the corresponding fit data after application of the tomographic algorithm.

Supplemental movies illustrate the path of data analysis. The movie ‘diamond_pci.mov’ shows the raw data. In file ‘diamond_rec_sub.mov’ the reconstructed phase maps after iterative refinement are summarized. In the reconstructed images the phase maps without shock wave were subtracted from the actual shock measurements enhancing the contrast for shock features.

References

1. The LCLS Design Study Group. *Linear coherent light source (LCLS) design study report*. Tech. Rep., SLAC-R-521, SLAC, Stanford (1998).
2. Ishikawa, T. *et al.* A compact X-ray free-electron laser emitting in the sub-ångström region. *Nat. Photonics* **6**, 540–544 (2012).
3. M. Altarelli *et al.* (ed.) *XFEL, The European X-Ray Free-Electron Laser (TDR)* (DESY, Hamburg, 2006).
4. Berrah, N. *et al.* Double-core-hole spectroscopy for chemical analysis with an intense X-ray femtosecond laser. *PNAS* **108**, 16912–16915 (2011).
5. Vinko, S. M. *et al.* Creation and diagnosis of a solid-density plasma with an x-ray free-electron laser. *Nature* **482**, 59–62 (2012).
6. Glover, T. E. *et al.* X-ray and optical wave mixing. *Nature* **488**, 603–608 (2012).
7. Chapman, H. N. *et al.* Femtosecond x-ray protein nanocrystallography. *Nature* **470**, 73 (2011).
8. Koopmann, R. *et al.* *In vivo* protein crystallization opens new routes in structural biology. *Nat. Methods* **9**, 259 (2012).
9. Davis, T., Gao, D., Gureyev, T., Stevenson, A. & Wilkins, S. Phase-contrast imaging of weakly absorbing materials using hard x-rays. *Nature* **373**, 595–598 (1995).
10. Cloetens, P., Barrett, R., Baruchel, J., Guigay, J.-P. & Schlenker, M. Phase objects in synchrotron radiation hard x-ray imaging. *J. Phys. D: Appl. Phys.* **29**, 133–146 (1996).
11. Cloetens, P. *et al.* Hard x-ray phase imaging using simple propagation of a coherent synchrotron radiation beam. *J. Phys. D: Appl. Phys.* **32**, A145–A151 (1999).
12. Mokso, R., Cloetens, P., Maire, E., Ludwig, W. & Buffière, J.-Y. Nanoscale zoom tomography with hard x rays using Kirkpatrick-Baez optics. *Appl. Phys. Lett.* **90**, 144104 (2007).
13. Giewekemeyer, K. *et al.* X-ray propagation microscopy of biological cells using waveguides as a quasipoint source. *Phys. Rev. A* **83**, 023804 (2011).
14. Lengeler, B. *et al.* Imaging by parabolic refractive lenses in the hard x-ray range. *J. Synchrotron Rad.* **6**, 1153–1167 (1999).
15. Schropp, A. *et al.* Developing a platform for high-resolution phase contrast imaging of high pressure shock waves in matter. In Moeller, S. P., Yabashi, M. & Hau-Riege, S. P. (eds.) *Proc. of SPIE*, vol. **8504**, 85040F (SPIE, San Diego, 2012).
16. Hicks, D. G. *et al.* High-precision measurements of the diamond Hugoniot in and above the melt region. *Phys. Rev. B* **78**, 174102 (2008).
17. Knudson, M. D., Desjarlais, M. P. & Dolan, D. H. Shock-wave exploration of the high-pressure phases of carbon. *Science* **322**, 1822–1825 (2008).
18. McWilliams, R. S. *et al.* Strength effects in diamond under shock compression from 0.1 to 1 TPa. *Phys. Rev. B* **81**, 014111 (2010).
19. Eggert, J. H. *et al.* Melting temperature of diamond at ultrahigh pressure. *Nat. Phys.* **6**, 40–43 (2010).
20. Smith, R. F. *et al.* Ramp compression of diamond to five terapascals. *Nature* **511**, 330–333 (2014).
21. Gabor, D. A new microscopic principle. *Nature* **161**, 777–778 (1948).
22. Schropp, A. *et al.* Full spatial characterization of a nanofocused x-ray free-electron laser beam by ptychographic imaging. *Sci. Rep.* **3**, 1633 (2013).
23. Wilkins, S., Gureyev, T., Gao, D., Pogany, A. & Stevenson, A. Phase-contrast imaging using polychromatic hard X-rays. *Nature* **384**, 335–338 (1996).
24. Vartanyants, I. A. *et al.* Coherence properties of individual femtosecond pulses of an x-ray free-electron laser. *Phys. Rev. Lett.* **107**, 144801 (2011).

25. Lee, S. *et al.* Single shot speckle and coherence analysis of the hard X-ray free electron laser LCLS. *Opt. Express* **21**, 24647–24664 (2013).
26. Born, M. & Wolf, E. *Principles of Optics* (Cambridge University Press, Cambridge, 1999).
27. Cowley, J. M. *Diffraction Physics* (Elsevier Science, 1995).
28. Mayo, S. *et al.* Quantitative X-ray projection microscopy: phase-contrast and multi-spectral imaging. *J. Microsc. (Oxford)* **207**, 79–96 (2002).
29. Seiboth, F. *et al.* Focusing XFEL SASE pulses by rotationally parabolic refractive x-ray lenses. In *J. Phys. Conf. Ser.* **vol. 499**, 012004 (2014).
30. Fienup, J. R. Phase retrieval algorithms: a comparison. *Appl. Opt.* **21**, 2758 (1982).
31. Gureyev, T. Composite techniques for phase retrieval in the Fresnel region. *Opt. Commun.* **220**, 49–58 (2003).
32. Schropp, A. *et al.* Scanning coherent x-ray microscopy as a tool for XFEL nanobeam characterization. In Klisnick, A & Menoni, C. S (ed.) *X-Ray Lasers and Coherent X-Ray Sources: Development and Applications X*, **vol. 8849**, 88490R (SPIE, San Diego, 2013).
33. Maiden, A. M. & Rodenburg, J. M. An improved ptychographical phase retrieval algorithm for diffractive imaging. *Ultramicroscopy* **109**, 1256–1262 (2009).
34. Clark, J. N. *et al.* Use of a complex constraint in coherent diffractive imaging. *Opt. Express* **18**, 1981–1993 (2010).

Acknowledgments

This work was performed at the Matter in Extreme Conditions (MEC) instrument of LCLS, supported by the DOE Office of Science, Fusion Energy Science under contract No. SF00515. This work was also supported by LCLS, a National User Facility operated by Stanford University on behalf of the U.S. Department of Energy, Office of Basic Energy Sciences. This work was funded by Volkswagen Foundation, the DFG under grant SCHR 1137/1-1, and by the German Ministry of Education and Research (BMBF) under grant number 05K13OD2. We would also like to thank the MEC team at SLAC, collaborating institutions, Bruno Lengeler for providing the CRL optics and Siegfried Glenzer for fruitful discussions.

Author Contributions

A.S., C.G.S. and J.B.H. conceived and coordinated the experiment. The setup was conceived and developed by A.S., C.G.S. and B.A. The beamline was set up and operated by H.J.L., B.N. and E.C.G. The experiment was carried out by A.S., R.H., V.M., J.P., F.S., H.J.L., B.N., E.C.G., U.Z. and C.G.S. The diamond samples were designed and provided by Y.P., D.G.H. and G.W.C. The data were analyzed by A.S., F.S., Y.P., G.W.C., J.S.W. and C.G.S. Numerical simulations were performed by A.H. and M.A.B. The manuscript was written by A.S., J.S.W., D.G.H. and C.G.S.

Additional Information

Supplementary information accompanies this paper at <http://www.nature.com/srep>

Competing financial interests: The authors declare no competing financial interests.

How to cite this article: Schropp, A. *et al.* Imaging Shock Waves in Diamond with Both High Temporal and Spatial Resolution at an XFEL. *Sci. Rep.* **5**, 11089; doi: 10.1038/srep11089 (2015).



This work is licensed under a Creative Commons Attribution 4.0 International License. The images or other third party material in this article are included in the article's Creative Commons license, unless indicated otherwise in the credit line; if the material is not included under the Creative Commons license, users will need to obtain permission from the license holder to reproduce the material. To view a copy of this license, visit <http://creativecommons.org/licenses/by/4.0/>